








On-the-fly machine learning potential accelerated accurate prediction of lattice thermal conductivity of metastable silicon crystals

Chunfeng Cui ^{1,*}, Yuwen Zhang ^{1,*}, Tao Ouyang ^{1,†}, Mingxing Chen ², Chao Tang ^{1,‡}, Qiao Chen ³,
Chaoyu He ¹, Jin Li ¹ and Jianxin Zhong ¹

¹Hunan Key Laboratory for Micro-Nano Energy Materials and Device and School of Physics and Optoelectronics, Xiangtan University, Xiangtan 411105, China

²College of Physics and Information Science, Hunan Normal University, Changsha 410081, China

³School of Computational Science & Electronics, Hunan Institute of Engineering, Xiangtan 411105, China



(Received 3 January 2023; accepted 6 March 2023; published 29 March 2023)

In this paper, we propose a convenient strategy to accelerate the evaluation of lattice thermal conductivity through combining phonon Boltzmann transport equation (PBTE) and on-the-fly machine learning potential (FMLP). The thermal conductivity of diamond silicon (*d*-Si) is evaluated firstly by density functional theory (DFT), FMLP, and empirical potential with PBTE, respectively. The results demonstrate the proposed strategy integrates the prediction accuracy of DFT and computational speed of empirical potential, breaking the dilemma of traditional thermal conductivity assessment schemes. Based on this, the efficient strategy is applied to predict thermal conductivity of 102 low-energy metastable silicon crystals with energies between *d*-Si and experimentally Si₂₄. Among them, the *Cmcm*-Si₁₆, *P6/mmm*-Si₃₆₋₂, *Pnma*-Si₃₂₋₂ are predicted to host lowest lattice thermal conductivity in *xx* (8.213 Wm⁻¹K⁻¹), *yy* (10.917 Wm⁻¹K⁻¹), and *zz* (11.807 Wm⁻¹K⁻¹) directions, respectively. Such low lattice thermal conductivity benefits from the combined effect of low phonon group velocity and intense phonon scattering caused by distorted *sp*³ hybrid states in these metastable silicon crystals. The findings presented in this work provide new candidates and insights of silicon-based materials with ultra-low thermal conductivity, which will greatly expand the applications in thermoelectric and thermal insulation fields.

DOI: [10.1103/PhysRevMaterials.7.033803](https://doi.org/10.1103/PhysRevMaterials.7.033803)

I. INTRODUCTION

As an essential performance parameter of materials, thermal conductivity plays a crucial role in thermoelectrics [1,2] and thermal management [3–5]. In order to achieve efficient design of heat-related functional materials and avoid dangerous situations from overheating, it is particularly necessary to establish an accurate and rapid strategy for evaluating thermal conductivity. However, rapid assessment to obtain precise lattice thermal conductivity will always be an extreme challenge both in theoretical and experimental models. Currently, combining the density functional theory (DFT) simulations and phonon Boltzmann transport equation (PBTE) is one of the most credible methods to evaluate the lattice thermal conductivity of bulk and low-dimensional materials [6–10]. Solving PBTE for obtaining the lattice thermal conductivity always takes the harmonic second-order interatomic force constants (2nd IFCs) and anharmonic third-order interatomic force constants (3rd IFCs) as inputs. Nevertheless, the 2nd IFCs, and especially the 3rd IFCs and high-order anharmonic force constants, are usually derived from at least hundreds or thousands of single-point DFT force calculations on the

corresponding supercell [11]. Obviously, evaluation of lattice thermal conductivity of materials through using the above approach usually requires expensive computational resources and time costs.

The empirical potential could accelerate the evaluation of interatomic interactions, and is extensively employed to explore the mechanical, thermal, and other physical and chemical properties of materials [12–15]. Unfortunately, their parameters are generally derived by fitting extremely limited experimental data (e.g., structural properties and elastic constants) from given structures, which leads to unsatisfactory accuracy of prediction of physical properties including the thermal conductivity based on the empirical potential. In recent years, Gaussian Approximation Potential (GAP) [16], Neuroevolutionary Machine Learning Potential (NEP) [17], Matrix Tensor Potential (MTP) [18], Deep Potential (DP) [19], etc., have emerged to greatly accelerate the evaluation of higher-order interatomic force constants while ensuring certain computational accuracy. The training set for training these machine learning potentials usually contains atomic coordinates, as well as information such as energy, force, and virial obtained from DFT calculations. The DFT calculation is usually performed by first-principles calculation software such as the Vienna Ab initio Simulation Package (VASP) [20], CP2K [21], and Quantum Espresso (QE) [22]. The recently introduced on-the-fly Machine Learning Potential (FMLP) of VASP automatically interpolates during

*These authors contributed equally to this work.

†Corresponding author: ouyangtao@xtu.edu.cn

‡Corresponding author: tang_chao@xtu.edu.cn

training between known training systems previously computed from scratch, predicting force field errors on freshly sampled structures in real-time based on Bayesian linear regression [23,24]. As an active learning strategy for dynamic structure generation during Molecular dynamics (MD) simulations, it has been proved to be particularly flexible and effective, and could achieve seamless integration into first-principles codes [25,26]. Meanwhile, it is identified to greatly reducing computational cost and manual intervention while maintaining the computational accuracy of first-principles methods [27].

Silicon-based materials are widely applied in transistors [28,29], integrated circuits [26,30], and photovoltaic devices [31,32] owing to their advantages of low raw material cost, mature preparation process, excellent electronic performance, and stability [33,34]. Among specific applications such as insulation and thermoelectric materials, low thermal conductivity materials are beneficial in blocking thermal transport and improving the thermoelectric figure of merit (ZT). Unfortunately, the high lattice thermal conductivity of diamond-configured silicon [35–37] (d -Si, the most thermodynamically stable phase at room temperature) limits its development in thermoelectrics and thermal insulation field. On considering the natural advantage of compatibility with modern silicon-based semiconductor processes [38–40], exploring metastable silicon crystal structures with low thermal conductivity is expected to dramatically expand and enhance the application in thermal transport field. Although a few investigations on the thermal properties of some metastable silicon crystals have been carried out, research in this area still lacks systematicity [39–42]. The major obstructions are attributed to the complexity of generating reasonable and well-stabilized silicon allotropes and the expensive computational resources required to obtain anharmonic force constants in evaluating lattice thermal conductivity.

Based on the above statement, we employ the recently introduced FMLP in VASP combined with ShengBTE software [11] to accelerate the prediction of lattice thermal conductivity of multiple low metastable silicon crystal structures, and a series of ideal configurations with ultralow thermal conductivity (e.g., $Cmcm$ -Si₁₆, $P6/mmm$ -Si₃₆₋₂, $Pnma$ -Si₃₂₋₂, etc.) are screened. The results confirm the method being an effective strategy to evaluate thermal conductivity of materials accurately and quickly, which will greatly facilitate the efficient design of thermoelectrics and thermal management in the future. The paper is organized as follows. In Sec. II, the calculation method and parameter settings of this work are introduced in detail, and the calculation flow chart is shown. In Sec. III, we present the phonon transport properties of d -Si calculated by employing DFT, FMLP, and empirical Tersoff potentials combined with ShengBTE software package to calculate under same parameter settings. The accuracy of the FMLP generated after MD simulation [23,43] in the accelerated evaluation of lattice thermal conductivity is verified by comparative analysis. Subsequently, 102 plausible and well-stabilized configurations are selected from 2585 silicon allotropes according to the energy criterion. After that, the 2nd IFCs and 3rd IFCs of the above 102 ideal configuration are calculated by using the FMLP method to accelerate the

evaluation of lattice thermal conductivity. In addition, the phonon mode information of metastable silicon crystal with extremely low lattice thermal conductivity is analyzed, and the underlying physical mechanism is revealed. Finally, we summarize the overall work in Sec. IV.

II. COMPUTATIONAL METHODOLOGY

A. Training of on-the-fly machine learning potential

The FMLP is generated based on structural dataset (Bravais lattice and atomic positions of the system and contains total energy, forces, and stress tensor calculated by first principles) identifying local structures around atoms [23,24,27]. The potential energy U_m^{FMLP} of a structure with N_a atoms [44] is approximated as the aggregate of local atomic potential energies U_i ,

$$U_m^{\text{FMLP}} = \sum_{i=1}^{N_a} U_i = \sum_{i=1}^{N_a} \sum_{i_B}^{N_B} w_{i_B} K(X_i, X_{i_B}). \quad (1)$$

The linear combination of weight factor w_{i_B} and kernel function $K(X_i, X_{i_B})$ is represented for each U_i . The kernel evaluates the similarity between the local configuration around atom i and the reference local configuration i_B . The energy, force, and stress tensor of structure is represented by ϕw , where ϕ is a matrix containing kernel function and the derivatives with respect to coordinates and lattice vector, and $w = \{w_{i_B}\}$. The energy, force, and stress tensor on all training configurations could be summarized as Φw , where Φ is the energy, force, and stress tensor on all training configurations collected. The parameters $w = [I/\delta_v^2 + \Phi^T \Phi/\delta_w^2]^{-1} \Phi^T Y/\delta_v^2$ and uncertainty $\sigma = \sigma_v^2 I + \phi^T [I/\sigma_w^2 + \Phi^T \Phi/\sigma_v^2]^{-1} \phi$ in predicting the energy, force, and stress tensor are determined based on Bayesian inference [45–47] to reproduce the first-principles energy, force, and stress tensor. The first-principles data of training configurations are retained in the vector Y , where I is the identity matrix. The σ_v^2 and σ_w^2 are determined using the evidence approximation method [45,46] to balance accuracy and robustness when training FMLP based on VASP. Each structural potential function is trained based on its own independent MD simulation, i.e., one structure has a corresponding FMLP. The results of calculating the lattice thermal conductivity of d -Si based on FMLP trained under MD simulations [23] with total steps ranging from 1000 to 10 000 (with an interval of 1000) are compared (see Sec. S1 of Supplemental Materials [48]). It can be found that the number of steps of pure DFT in MD simulations is extremely small (about 33 steps on average), however, the lattice thermal conductivity is well predicted (about 154.93 Wm⁻¹K⁻¹ on average) based on 10 different sets of simulated cases. According to the above experimental results, MD simulation training parameters of this work are set as follows: MD is performed with the isothermal-isobaric (NPT) condition at 300 K and 0 Pa. MD steps are 5000 steps with a time step of 1 fs, supercell has a length of no less than 25 Å in all three lattice directions, cutoff energy of the plane wave is 450 eV, cutoff distance is 6 Å, and Monkhorst-Pack meshes are set to $1 \times 1 \times 1$.

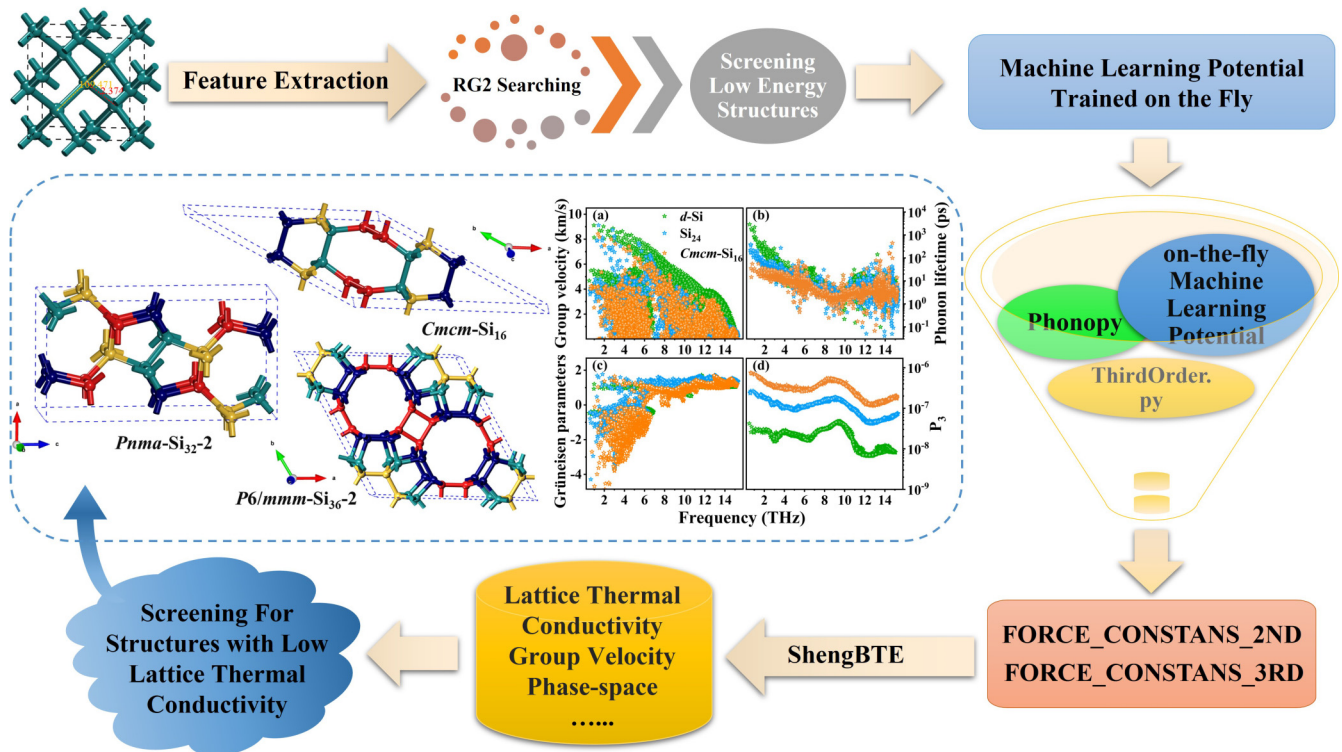


FIG. 1. The flow chart of FMLP combined with ShengBTE software to predict lattice thermal conductivity of various low-energy metastable silicon crystal structures. In the dashed boxes, the left inset shows the crystal structures of three metastable silicon ($Cmc-Si_{16}$, $P6/mmm-Si_{36-2}$, and $Pnma-Si_{32-2}$) with extremely low lattice thermal conductivity, and the right inset shows the phonon transport properties of $Cmc-Si_{16}$. The spheres with different colors represent unequal silicon atoms.

B. Generation of candidate structures

By using the crystal structure search software RG^2 [49] based on random strategy, group theory, and graph theory, taking the d -Si configuration with $Fd-3m$ symmetry as the starting point, 2585 silicon allotropes are quickly obtained. The first-principles calculations are performed through using the Projected Augmented Wave (PAW) [50] method implemented in the VASP [20]. The Perdew-Burke-Ernzerhof (PBE) [51] generalized gradient approximation (GGA) [52] is utilized to describe the ion-electron interactions. In our calculation, the cutoff energy of the plane wave is set as 450 eV and the energy convergence criterion for the electron self-consistent field is set as 10^{-7} eV until the residual stress on each atom is less than 0.001 eV/Å [51]. The Brillouin zone is sampled using Monkhorst-Pack [53] k meshes. The k -point grid spacing in each direction of reciprocal space is within $0.03 \times 2\pi$ Å $^{-1}$ generated by VASPKIT [54] code. Taken the cohesion energy as a criterion, 102 reasonable and well-stabilized silicon crystal structures are finally screened between the experimentally prepared d -Si and Si_{24} [55]. In addition, the band-gap characteristics of 2585 silicon allotropes are qualitatively counted at the DFT-PBE level.

C. Evaluation of lattice thermal conductivity

Based on FMLP combined with Phonopy [56] and third-order.py code [57], 2nd IFCs and 3rd IFCs could be quickly obtained as input files for the ShengBTE [11] software in order to derive the phonon transport properties. The 2nd IFCs

and 3rd IFCs are calculated with the supercell size not less than 20 Å in all three directions with a cutoff distance of 6 Å. The lattice thermal conductivity could be described as [11]

$$\kappa_i^{xy} = \frac{1}{k_B T^2 \Omega N} \sum_{\lambda} f_0(\omega_{\lambda})(f_0(\omega_{\lambda}) + 1)(\hbar \omega_{\lambda})^2 v_{\lambda}^x v_{\lambda}^y \tau_{\lambda}, \quad (2)$$

where k_B , T , Ω , \hbar , and N are the Boltzmann constant, temperature, volume of unit cell, Planck constant, and the number of wave-vector points in the first Brillouin zone; ω_{λ} , v_{λ} , and τ_{λ} are the angular frequency, group velocity, and relaxation time of phonon mode λ ; x and y are the Cartesian components of x , y , or z , and $f_0(\omega_{\lambda})$ is the equilibrium Bose-Einstein distribution function. The k mesh with $k_x a \approx k_y b \approx k_z c$ not less than 80 Å are used in ShengBTE for sampling the first Brillouin zone to ensure the convergence of thermal conductivity. The complete computational flow is shown in Fig. 1.

III. RESULTS AND DISCUSSION

Taken the d -Si as an example, we firstly examine the reliability of FMLP combined with ShengBTE in accelerating the evaluation of lattice thermal conductivity. Figures 2(a) and 2(b) illustrate the per-atom energy and atomic force of multiple silicon configurations calculated by the FMLP and DFT. It is obvious that the calculation date of energy and atomic force obtained from the FMLP method possess excellent linear relationship (the slope is approximately 0.5) with the results from the DFT method. The corresponding root mean square errors (RMSE) of energy and atomic force are estimated as

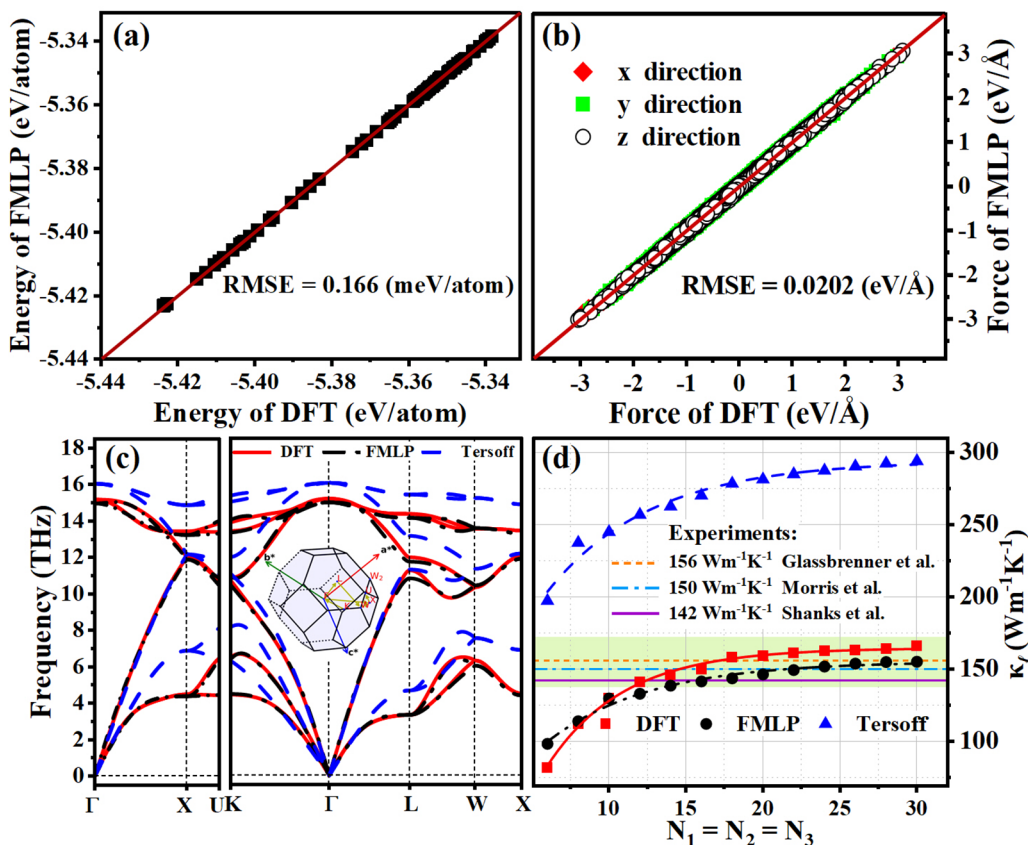


FIG. 2. The comparison of (a) per-atom energy and (b) atomic force when FMLP and DFT calculate multiple silicon configurations. (c) The phonon dispersion of *d*-Si based on DFT, FMLP, and empirical Tersoff potential, respectively. (d) The room temperature lattice thermal conductivity of *d*-Si in experiments and theoretical calculations, and based on DFT, FMLP, and empirical Tersoff potential combined with ShengBTE package, respectively.

0.166 meV/atom and 0.0202 eV/Å. Such extremely small RMSE values indicate that FMLP has comparable accuracy in regenerating potential energy surface compared with DFT calculation. That is to say, the accelerated calculation based on FMLP could ensure the accurate prediction of multitarget physical properties. The phonon dispersion contains a variety of phonon information, including phonon band structure, group velocity, and phonon scattering phase space, which is an important prerequisite for accurately evaluating the phonon transport properties of materials. Based on the FMLP combined with Phonopy software, the phonon dispersion of *d*-Si is calculated, and the result is depicted in Fig. 2(c). Here the calculation data based on the DFT and empirical Tersoff potential [58] is given as well for comparison. One can note clearly that the phonon dispersion predicted by the empirical Tersoff potential (blue dotted line) deviates considerably from the DFT calculations (red solid line), while that obtained from the FMLP (black double-dotted line) are in excellent agreement with the DFT results owing to the accurate energy and atomic force calculation. Afterwards, the lattice thermal conductivity of *d*-Si obtained for different situations is comparatively analyzed to obviously demonstrate the accuracy and efficiency of FMLP-based calculations. As shown in Fig. 2(d), the green reference area (the floating range is 137–172 Wm⁻¹K⁻¹) is plotted according to the lattice thermal conductivities of *d*-Si calculated based on DFT from several references [39,59,60],

and the reference lines of the experimental data are the orange dotted line (156 Wm⁻¹K⁻¹) [35], blue double-dotted line (150 Wm⁻¹K⁻¹) [36], and purple solid line (142 Wm⁻¹K⁻¹) [37]. Undoubtedly, the empirical Tersoff potential evidently overestimates the lattice thermal conductivity of *d*-Si, while the lattice thermal conductivity evaluated from the FMLP combined with ShengBTE software falls perfectly in the DFT-based predicted and experimental data interval. These results confirm that FMLP combined with ShengBTE is a reliable strategy to evaluate the thermal conductivity of materials. Taken the Silicene and 2H-Si as representatives, we further demonstrate the robustness of the strategy proposed in this work, and the detailed content is provided in Sec. S2 of the Supplemental Materials [48]. On considering the negligible computation time when calculating the 2nd IFCs and 3rd IFCs based on FMLP compared to DFT (supporting information could be found in Sec. S3 of the Supplemental Materials [48]), such strategy could be utilized well to accelerate the accurate evaluation of lattice thermal conductivity.

To systematically investigate the thermal transport properties of silicon allotropes, one should construct the structure database of metastable silicon crystals firstly. In this work, we mainly focus on the metastable silicon crystals with *sp*³ hybridization state. Thus, the fundamental input information is learned from the *d*-Si [bonding list (Si: Si Si Si Si), average bond length is 2.366 Å, average bond angle is 109.47°],

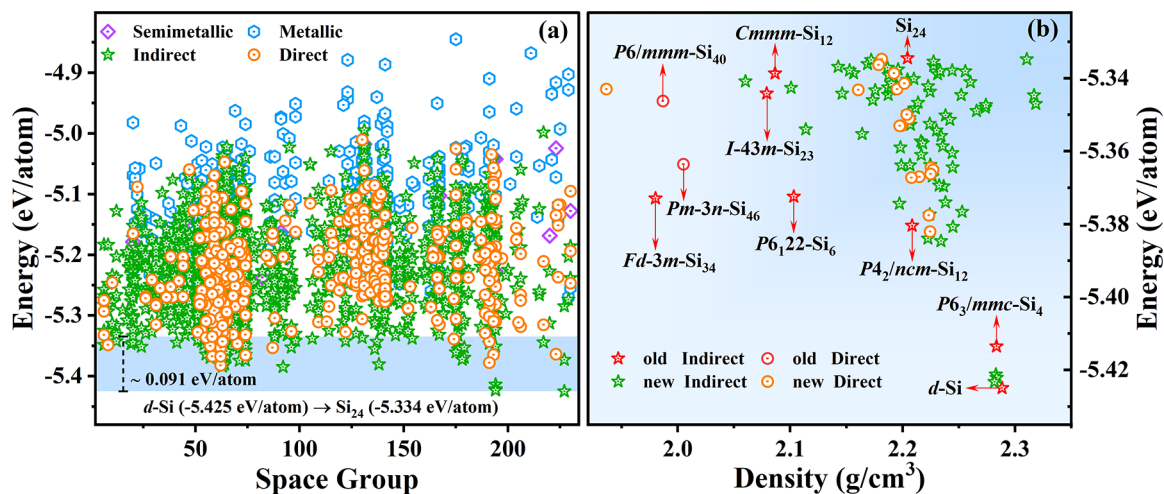


FIG. 3. (a) The total energy per atom and the basic electronic property as a function of their corresponding number of space group for 2585 silicon allotropes. (b) 102 metastable silicon crystal structures with reasonable and good stability in the low energy region. A few structures are old structures (marked in red) that have been predicted earlier.

and we obtain 2585 silicon allotropes by means of the crystal structure search software RG^2 . The input parameters for searching for silicon allotropes employing RG^2 can be found in the Supplemental Material [48], Sec. S4 for interested readers. The total energy per atom and basic electronic property as a function of their corresponding number of space groups are depicted in Fig. 3(a). Generally speaking, if total energy per atom of system is lower, kinetic energy of atoms is lower and the bonds are less likely to be broken, implying the structure is more stable and possesses high probability of existence under natural or prepared in experiment. On the fundamental of this criterion, we mainly focus on the silicon allotropes with total energy lower than the experimentally prepared Si_{24} (-5.334 eV/atom). Among the 2585 candidates, we merely screen out 102 metastable silicon crystals with total energy located between the $d\text{-Si}$ and Si_{24} , which are shown in Fig. 3(b). According to the space group (Sg) and number of atoms in the primitive cell (Si_n), these low-energy silicon structures are named as $\text{Sg-Si}_n\text{-O}$, and the label O (O is an integer starting from 1) is utilized to distinguish the silicon allotropes with same Sg and Si_n . Such naming strategy is convenient for managing the metastable silicon crystal family and helping us to check the structure repetitiveness. Through comparing the structure data in open-source materials database Materials Project [61], 10 structures are old structures [marked in red symbols in Fig. 3(b)] that have been predicted in earlier works. All the remaining 92 structure are semiconductors, containing 18 direct band-gap semiconductors and 74 indirect band-gap semiconductors. As we know, semiconductors always possess better thermoelectric performance than metal. That is to say, these new 92 metastable silicon-based semiconductors provide fruitful potential candidates for thermoelectrics. Meanwhile, the 18 direct band gap silicon-based semiconductors also offer potential suitable candidates for photovoltaics. More detail structure information for $d\text{-Si}$, Si_{24} , and 102 metastable silicon crystal structures is prepared as Supplemental Material [48], Sec. S5 for interested readers.

By utilizing the FMLP combined with ShengBTE, in Fig. 4 we depict the lattice thermal conductivity versus the space

group of 102 metastable silicon crystal structures. More detailed information is provided in Sec. S5 of the Supplemental Materials [48]. It can be seen from Figs. 4(a) to 4(c) that the lattice thermal conductivity of most metastable silicon crystal structures is concentrated between $20\text{--}40 \text{ Wm}^{-1}\text{K}^{-1}$ along three crystal directions. The average lattice thermal conductivity is provided in Fig. 4(d) as well. One can know that the average lattice thermal conductivity of the 102 metastable silicon structures along the xx , yy , and zz directions are 29.519 , 30.541 , and $31.397 \text{ Wm}^{-1}\text{K}^{-1}$, respectively. Among the 102 metastable silicon structures, we screen out three structures with the lowest unidirectional lattice thermal conductivity in xx , yy , and zz directions, i.e., $Cmcm\text{-Si}_{16}$ ($8.213 \text{ Wm}^{-1}\text{K}^{-1}$

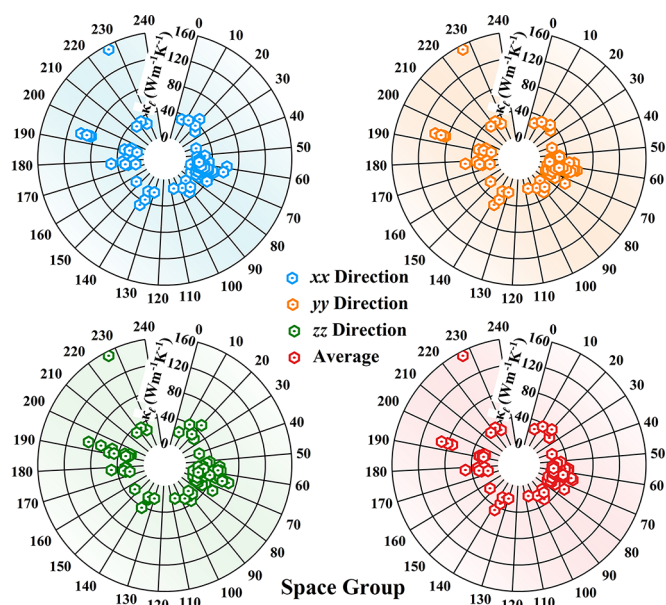


FIG. 4. The lattice thermal conductivities along the xx , yy , and zz directions for $d\text{-Si}$, Si_{24} , and 102 metastable silicon crystal structures, and average lattice thermal conductivities for each structure at room temperature are distributed by space group.

TABLE I. The lattice parameters of three metastable silicon ($Cmcm$ -Si₁₆, $P6/mmm$ -Si₃₆₋₂, and $Pnma$ -Si₃₂₋₂) with extremely low lattice thermal conductivity.

Name	a (Å)	b (Å)	c (Å)	α	β	γ	κ_{l-xx}	κ_{l-yy}	κ_{l-zz}
$Cmcm$ -Si ₁₆	13.797	13.797	3.869	90°	90°	153°	8.213	11.839	35.528
$P6/mmm$ -Si ₃₆₋₂	15.606	15.606	3.864	90°	90°	120°	10.912	10.912	46.502
$Pnma$ -Si ₃₂₋₂	7.447	6.481	14.237	90°	90°	90°	24.242	29.838	11.807

in xx direction), $P6/mmm$ -Si₃₆₋₂ (10.917 Wm⁻¹K⁻¹ in yy direction), and $Pnma$ -Si₃₂₋₂ (11.807 Wm⁻¹K⁻¹ in zz direction). The lattice thermal conductivity of $Cmcm$ -Si₁₆, $P6/mmm$ -Si₃₆₋₂, and $Pnma$ -Si₃₂₋₂ as a function of temperatures are presented in Sec. S6 of the Supplemental Materials [48]. Because of the enhanced phonon-phonon scattering with temperature, their lattice thermal conductivity decreases with the increase of temperature, which is a common thermal phenomenon in most bulk materials. Meanwhile, from Fig. 4 one can also note that the metastable silicon crystal structures with extremely low lattice thermal conductivity mostly possess small space group numbers. This is mainly originated from the fact that the lower symmetry will enhance the avoid-crossing behavior of phonon branches and reduction of phonon degeneracy [62], which gives rise to the stronger anharmonic lattice vibrations and low thermal conductivity. The lattice parameters, lattice thermal conductivity in three directions, and crystal structures of the above three structures are shown in Table I and Fig. 1, respectively. The more detailed atomic structure information is provided in Sec. S7 of the Supplemental Materials [48].

The dynamical, thermal, and mechanical stability of $Cmcm$ -Si₁₆, $P6/mmm$ -Si₃₆₋₂, and $Pnma$ -Si₃₂₋₂ are verified in order to ensure a rational practical application. As shown in Figs. 5(a) to 5(c), the phonon dispersion spectra obtained un-

der DFT, FMLP, and empirical Tersoff potential calculations for all three configurations are without imaginary frequency, indicating they are dynamically stable. It is worth mentioning that the phonon spectra of the three structures obtained based on the FMLP accelerated calculations are basically consistent with respect to the DFT, further validating the reliability of the evaluation of FMLP accelerated of 2nd IFCs and 3rd IFCs. Additionally, the comparisons of per-atom energy and atomic force when using FMLP and DFT calculations is provided in Sec. S8 of the Supplemental Materials [48]. The root mean square errors of energy (atomic force) are estimated as 0.103 meV/atom (0.0284 eV/Å), 0.258 meV/atom (0.0354 eV/Å), and 0.153 meV/atom (0.0374 eV/Å) for $Cmcm$ -Si₁₆, $P6/mmm$ -Si₃₆₋₂, and $Pnma$ -Si₃₂₋₂, respectively. As for the thermal stability, one can see from Figs. 5(d) to 5(f) that after running MD simulation for 50 000 fs at room temperature the final structural configurations of these three metastable silicon structures are maintained without damage. The energy of the system over time fluctuates only slightly in the range of stable values, further demonstrating the thermal stability. In addition, the $Cmcm$ -Si₁₆, $P6/mmm$ -Si₃₆₋₂, and $Pnma$ -Si₃₂₋₂ all possess great mechanical stability. Their elastic constants are all in accordance with the mechanical stability criteria in the corresponding systems, and the detailed process is also provided in Sec. S9 of the Supplemental Materials [48].

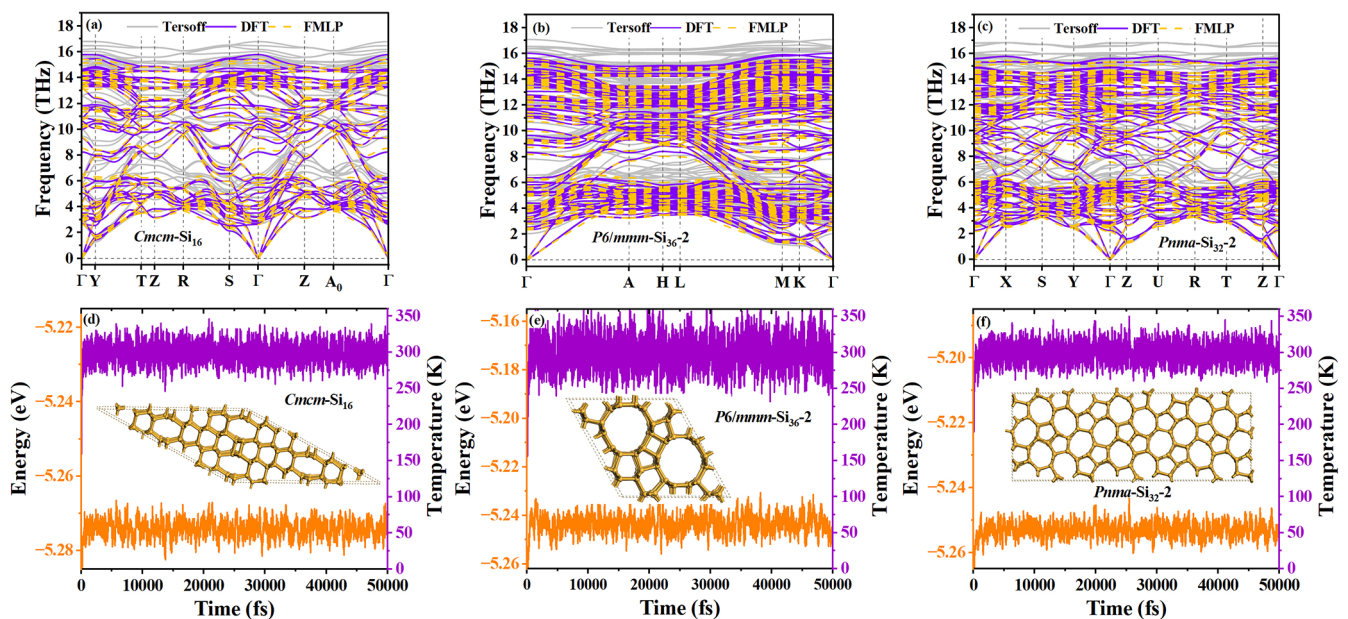


FIG. 5. The phonon dispersion of (a) $Cmcm$ -Si₁₆, (b) $P6/mmm$ -Si₃₆₋₂, and (c) $Pnma$ -Si₃₂₋₂ based on DFT, FMLP, and empirical Tersoff potential, respectively. The MD simulations of (d) $Cmcm$ -Si₁₆, (e) $P6/mmm$ -Si₃₆₋₂, and (f) $Pnma$ -Si₃₂₋₂ at 300 K for 50 000 fs. The structures in the inset are the final configurations after MD simulations are performed.

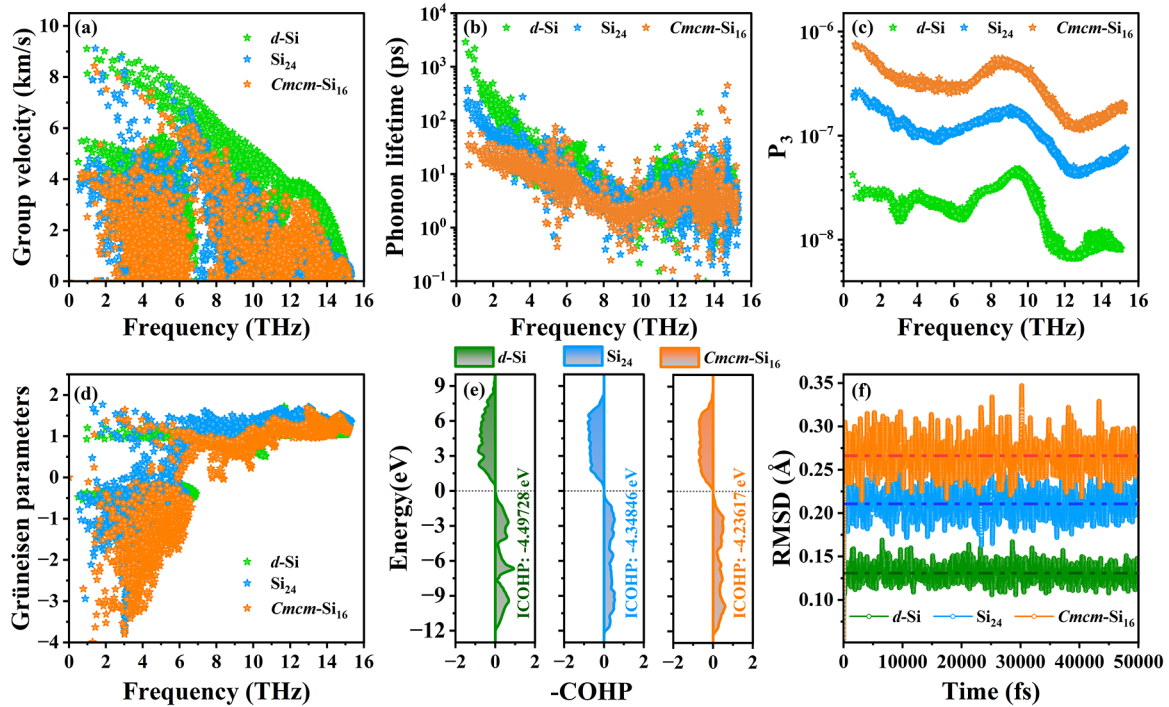


FIG. 6. The (a) Group velocity, (b) phonon lifetime, (c) three-phonon scattering phase space, and (d) Grüneisen parameter versus frequency for d -Si, Si_{24} , and Cmcm-Si_{16} versus frequency at room temperature, (e) root-mean-square deviation of atomic positions, and (f) the integration of Crystal Orbital Hamilton Population for d -Si, Si_{24} , and Cmcm-Si_{16} .

To understand the underlying physical mechanisms of the extremely low lattice thermal conductivity, we decompose the phonon mode information of the above-mentioned three metastable silicon structures. In this work, the structure Cmcm-Si_{16} with the lowest lattice thermal conductivity in the xx direction is taken as an example for specific analysis. The phonon transport properties for $P6/mmm\text{-Si}_{36}\text{-2}$ and $Pnma\text{-Si}_{32}\text{-2}$ with the lowest lattice thermal conductivity in the yy and zz directions are also presented (see Sec. S10 of the Supplemental Materials [48]). It can be seen from Fig. 6(a) that the phonon group velocity of Cmcm-Si_{16} is significantly slower than that of d -Si, which is one of the sources for its low lattice thermal conductivity. This is mainly due to the presence of more flat phonon modes in the phonon dispersion spectrum of Cmcm-Si_{16} relative to d -Si, and the phonon group velocity is related to the slope of the phonon modes. The phonon group velocity of Cmcm-Si_{16} is only slightly lower than that of Si_{24} , yet has a much lower lattice thermal conductivity, which implies that more significant factors than the group velocity are dominant. The phonon lifetime is another important parameter in determining the lattice thermal conductivity, and it can be found from Fig. 6(b) that the phonon lifetime of Cmcm-Si_{16} is obviously lower than that of d -Si and Si_{24} . The phonon lifetime shows a positive correlation with the lattice thermal conductivity, and its magnitude is mainly determined by two factors: scattering probability and scattering intensity. Therefore, the phonon scattering mechanisms involved are further analyzed in detail from both perspectives.

As shown in Fig. 6(c), Cmcm-Si_{16} possesses significantly larger scattering phase space than d -Si and Si_{24} , and larger scattering space means more phonon scattering channels, resulting in shorter phonon relaxation time. This phenomenon

is mainly owing to the mixing of acoustic and optical phonon modes of Cmcm-Si_{16} , where phonon scattering is more likely to satisfy the requirements of energy conservation and quasi-momentum conservation, resulting in a larger scattering phase space in Cmcm-Si_{16} . The phonon scattering intensity is quantified by the Grüneisen parameter, and it can be seen from Fig. 6(d) that the average Grüneisen parameter (absolute value) of Cmcm-Si_{16} is higher than that of d -Si and Si_{24} , indicating that it has a stronger degree of phonon scattering. Atoms are only allowed to be displaced from equilibrium by the natural energy of thermal fluctuations, hence the stronger the phonon-phonon scattering occurs the further the atom deviates from its equilibrium position. The root-mean-square deviation (RMSD) [63,64] could be used to quantify the amplitude of atomic vibrations, reflecting the distance of the atom from its equilibrium position and the sensitivity of the atom to the potential energy surface. The RMSDs of d -Si, Si_{24} , and Cmcm-Si_{16} are calculated separately by employing Visual Molecular Dynamics (VMD) [65]. The larger RMSD of Cmcm-Si_{16} (0.266 Å) relative to d -Si (0.131 Å) and Si_{24} (0.211 Å) in Fig. 6(e) further confirms its strong phonon anharmonicity. Moreover, this means that Cmcm-Si_{16} deviates further from the equilibrium position in the lattice vibration and therefore requires more energy to recover the deviation, i.e., weaker interatomic bonding. In contrast to the perfect tetrahedra in d -Si (all bond lengths are 2.366 Å and all bond angles are 109.47°), the atoms in Cmcm-Si_{16} form tetrahedral connections with distorted sp^3 hybrid, and bond lengths range between 2.345 Å \sim 2.403 Å and bond angles range between $90^\circ \sim 122.15^\circ$. The integration of Crystal Orbital Hamilton Populations (ICOHP) [66] value could indicate bonding state occupation by the orbital electrons,

thus reflecting the strength of the interatomic bonding. The ICOHP is calculated by employing the LOBSTER [67] code, and as can be seen in Fig. 6(f), *Cmcm*-Si₁₆ (-4.23617 eV) has a higher ICOHP value than Si₂₄ (-4.34846 eV) and *d*-Si (-4.49728 eV). This implies that *Cmcm*-Si₁₆ has smaller bonding state occupation by the orbital electrons, i.e., weaker interatomic bonding, which resulted in lower lattice thermal conductivity [68,69]. Hence, the slow phonon group velocity and extremely strong phonon-phonon scattering (scattering intensity and scattering probability) caused by the distorted *sp*³ hybrid states in *Cmcm*-Si₁₆ together attribute to its low lattice thermal conductivity.

IV. CONCLUSION

In summary, we demonstrate that PBTE combined with FMLP introduced in VASP is an effective strategy for accurately and rapidly assessing the thermal conductivity of materials, and applied the approach to evaluate the thermal conductivity of metastable silicon crystals in batches. The extremely minor differences in energy per atom, atomic force, and phonon dispersion under FMLP and DFT calculations suggest that FMLP could be well suited for accelerated lattice thermal conductivity evaluation. The lattice thermal conductivity of *d*-Si calculated based on FMLP falls perfectly in the DFT-based predicted and experimental interval showing excellent accuracy. The lattice thermal conductivity of the 102 metastable silicon crystal structures [energy per atom is between *d*-Si (-5.425 eV/atom) and experimentally prepared Si₂₄ (-5.334 eV/atom)] are predicted through FMLP combined with ShengBTE software, and a series of well-stabilized ultralow lattice thermal conductivity configurations are screened out. Among them, the silicon allotropes with the lowest lattice thermal conductivity in *xx*, *yy*, and *zz* directions are *Cmcm*-Si₁₆ (8.213 Wm⁻¹K⁻¹), *P6/mmm*-Si₃₆₋₂ (10.917

Wm⁻¹K⁻¹), and *Pnma*-Si₃₂₋₂ (11.807 Wm⁻¹K⁻¹), and they are demonstrated to be dynamically, thermally, and mechanically stable. Furthermore, the potential physical mechanisms for its extremely low lattice thermal conductivity are systematically explored by calculating its phonon group velocity and phonon lifetime. It is revealed that such ultralow lattice thermal conductivity benefits from the combined effect of low phonon group velocity and intense phonon scattering caused by the distorted *sp*³ hybrid state. The above findings indicate that the PBTE combined with FMLP introduced in VASP is an effective strategy to evaluate thermal conductivity accurately and rapidly in batches, which will considerably facilitate the research on thermal transport of various materials. Meanwhile, the metastable silicon crystal structures with extremely low thermal conductivity will most probably be prepared experimentally, expanding the practical applications of silicon-based materials in thermoelectric and thermal insulation.

ACKNOWLEDGMENTS

This work is supported by the Youth Science and Technology Talent Project of Hunan Province (Grant No. 2022RC1197), the National Natural Science Foundation of China (Grants No. 11974299 and No. 11974300), the Scientific Research Foundation of Education Bureau of Hunan Province (Grants No. 20B582, No. 20K127, No. 19C1746, and No. 20A503), the Science Fund for Distinguished Young Scholars of Hunan Province of China (Grant No. 2021JJ10036), the Hunan Provincial Innovation Foundation for Postgraduate (Grant No. CX20220544), and the Program for Changjiang Scholars and Innovative Research Team in University (Grant No. IRT13093).

-
- [1] J. He and T. M. Tritt, Advances in thermoelectric materials research: Looking back and moving forward, *Science* **357**, eaak9997 (2017).
 - [2] X. Yang, C. Wang, R. Lu, Y. Shen, H. Zhao, J. Li, R. Li, L. Zhang, H. Chen, T. Zhang, and X. Zheng, Progress in measurement of thermoelectric properties of micro/nano thermoelectric materials: A critical review, *Nano Energy* **101**, 109253 (2022).
 - [3] Y. Guo, H. Qiu, K. Ruan, S. Wang, Y. Zhang, and J. Gu, Flexible and insulating silicone rubber composites with sandwich structure for thermal management and electromagnetic interference shielding, *Compos. Sci. Technol.* **219**, 109253 (2022).
 - [4] Y. Han, K. Ruan, and J. Gu, Janus (BNNS/ANF)-(AgNWs/ANF) thermal conductivity composite films with superior electromagnetic interference shielding and Joule heating performances, *Nano Res.* **15**, 4747 (2022).
 - [5] Y. He and T. Xie, Advances of thermal conductivity models of nanoscale silica aerogel insulation material, *Appl. Therm. Eng.* **81**, 28 (2015).
 - [6] A. Nabovati, D. P. Sellan, and C. H. Amon, On the lattice Boltzmann method for phonon transport, *J. Comput. Phys.* **230**, 5864 (2011).
 - [7] D. Qin, P. Yan, G. Ding, X. Ge, H. Song, and G. Gao, Monolayer PdSe₂: A promising two-dimensional thermoelectric material, *Sci. Rep.* **8**, 2764 (2018).
 - [8] T. Tadano and S. Tsuneyuki, Self-consistent phonon calculations of lattice dynamical properties in cubic SrTiO₃ with first-principles anharmonic force constants, *Phys. Rev. B* **92**, 054301 (2015).
 - [9] J. Zhang, H. J. Liu, L. Cheng, J. Wei, J. H. Liang, D. D. Fan, J. Shi, X. F. Tang, and Q. J. Zhang, Phosphorene nanoribbon as a promising candidate for thermoelectric applications, *Sci. Rep.* **4**, 6452 (2014).
 - [10] B. Mortazavi, E. V. Podryabinkin, I. S. Novikov, T. Rabczuk, X. Zhuang, and A. V. Shapeev, Accelerating first-principles estimation of thermal conductivity by machine-learning interatomic potentials: A MTP/ShengBTE solution, *Comput. Phys. Commun.* **258**, 107583 (2021).
 - [11] W. Li, J. Carrete, N. A. Katcho, and N. Mingo, ShengBTE: A solver of the Boltzmann transport equation for phonons, *Comput. Phys. Commun.* **185**, 1747 (2014).
 - [12] P. Norouzzadeh and D. J. Singh, Thermal conductivity of single-layer WSe₂ by a Stillinger-Weber potential, *Nanotechnology* **28**, 075708 (2017).

- [13] X. Zhang, H. Xie, M. Hu, H. Bao, S. Yue, G. Qin, and G. Su, Thermal conductivity of silicene calculated using an optimized Stillinger-Weber potential, *Phys. Rev. B* **89**, 054310 (2014).
- [14] Z. Fan, Y. Wang, X. Gu, P. Qian, Y. Su, and T. Ala-Nissila, A minimal Tersoff potential for diamond silicon with improved descriptions of elastic and phonon transport properties, *J. Phys.: Condens. Matter* **32**, 135901 (2020).
- [15] A. Kinaci, J. B. Haskins, C. Sevik, and T. Çağın, Thermal conductivity of BN-C nanostructures, *Phys. Rev. B* **86**, 115410 (2012).
- [16] A. P. Bartok, M. C. Payne, R. Kondor, and G. Csanyi, Gaussian Approximation Potentials: The Accuracy of Quantum Mechanics, without the Electrons, *Phys. Rev. Lett.* **104**, 136403 (2010).
- [17] Z. Fan, Z. Zeng, C. Zhang, Y. Wang, K. Song, H. Dong, Y. Chen, and T. Ala-Nissila, Neuroevolution machine learning potentials: Combining high accuracy and low cost in atomistic simulations and application to heat transport, *Phys. Rev. B* **104**, 104309 (2021).
- [18] Y. Ouyang, C. Yu, J. He, P. Jiang, W. Ren, and J. Chen, Accurate description of high-order phonon anharmonicity and lattice thermal conductivity from molecular dynamics simulations with machine learning potential, *Phys. Rev. B* **105**, 115202 (2022).
- [19] H. Wang, L. Zhang, J. Han, and W. E, DeePMD-kit: A deep learning package for many-body potential energy representation and molecular dynamics, *Comput. Phys. Commun.* **228**, 178 (2018).
- [20] G. Kresse and J. Furthmüller, Efficient iterative schemes for ab initio total-energy calculations using a plane-wave basis set, *Phys. Rev. B* **54**, 11169 (1996).
- [21] J. Hutter, M. Iannuzzi, F. Schiffmann, and J. VandeVondele, CP2K: atomistic simulations of condensed matter systems, *WIREs Comput. Mol. Sci.* **4**, 15 (2014).
- [22] P. Giannozzi, O. Barone, P. Bonfa, D. Brunato, R. Car, I. Carnimeo, C. Cavazzoni, S. de Gironcoli, P. Delugas, F. F. Ruffino, A. Ferretti, N. Marzari, I. Timrov, A. Urru, and S. Baroni, Quantum ESPRESSO toward the exascale, *J. Chem. Phys.* **152**, 154105 (2020).
- [23] R. Jinnouchi, F. Karsai, and G. Kresse, On-the-fly machine learning force field generation: Application to melting points, *Phys. Rev. B* **100**, 014105 (2019).
- [24] R. Jinnouchi, F. Karsai, C. Verdi, R. Asahi, and G. Kresse, Descriptors representing two- and three-body atomic distributions and their effects on the accuracy of machine-learned inter-atomic potentials, *J. Chem. Phys.* **152**, 234102 (2020).
- [25] E. V. Podryabinkin and A. V. Shapeev, Active learning of linearly parametrized interatomic potentials, *Comput. Mater. Sci.* **140**, 171 (2017).
- [26] T. Komljenovic, M. Davenport, J. Hulme, A. Y. Liu, C. T. Santis, A. Spott, S. Srinivasan, E. J. Stanton, C. Zhang, and J. E. Bowers, Heterogeneous silicon photonic integrated circuits, *J. Lightwave Technol.* **34**, 20 (2016).
- [27] R. Jinnouchi, J. Lahnsteiner, F. Karsai, G. Kresse, and M. Bokdam, Phase Transitions of Hybrid Perovskites Simulated by Machine-Learning Force Fields Trained on the Fly with Bayesian Inference, *Phys. Rev. Lett.* **122**, 225701 (2019).
- [28] V. Adinolfi and E. H. Sargent, Photovoltage field-effect transistors, *Nature (London)* **542**, 324 (2017).
- [29] K. Tomioka, M. Yoshimura, and T. Fukui, A III-V nanowire channel on silicon for high-performance vertical transistors, *Nature (London)* **488**, 189 (2012).
- [30] M. J. R. Heck, J. F. Bauters, M. L. Davenport, J. K. Doylend, S. Jain, G. Kurczveil, S. Srinivasan, Y. Tang, and J. E. Bowers, Hybrid silicon photonic integrated circuit technology, *IEEE J. Sel. Top. Quantum Electron.* **19**, 6100117 (2013).
- [31] D. Adachi, J. L. Hernández, and K. Yamamoto, Impact of carrier recombination on fill factor for large area heterojunction crystalline silicon solar cell with 25.1% efficiency, *Appl. Phys. Lett.* **107**, 233506 (2015).
- [32] C. Battaglia, A. Cuevas, and S. De Wolf, High-efficiency crystalline silicon solar cells: Status and perspectives, *Energy Environ. Sci.* **9**, 1552 (2016).
- [33] J. Kim, M. Lee, H. J. Shim, R. Ghaffari, H. R. Cho, D. Son, Y. H. Jung, M. Soh, C. Choi, S. Jung, K. Chu, D. Jeon, S.-T. Lee, J. H. Kim, S. H. Choi, T. Hyeon, and D.-H. Kim, Stretchable silicon nanoribbon electronics for skin prosthesis, *Nat. Commun.* **5**, 5747 (2014).
- [34] H. Wu, G. Zheng, N. Liu, T. J. Carney, Y. Yang, and Y. Cui, Engineering empty space between Si nanoparticles for lithium-ion battery anodes, *Nano Lett.* **12**, 904 (2012).
- [35] C. J. Glassbrenner and G. A. Slack, Thermal conductivity of silicon and germanium from 3° K to the melting point, *Phys. Rev.* **134**, A1058 (1964).
- [36] R. G. Morris and J. G. Hust, Thermal conductivity measurements of silicon from 30° to 425°C, *Phys. Rev.* **124**, 1426 (1961).
- [37] H. R. Shanks, P. D. Maycock, P. H. Sidles, and G. C. Danielson, Thermal conductivity of silicon from 300 to 1400°K, *Phys. Rev.* **130**, 1743 (1963).
- [38] K. Wang, S. Pei, Z. He, L.-a. Huang, S. Zhu, J. Guo, H. Shao, and J. Wang, Synthesis of a novel porous silicon microsphere@carbon core-shell composite via in situ MOF coating for lithium ion battery anodes, *Chem. Eng. J.* **356**, 272 (2019).
- [39] T. Ouyang, P. Zhang, H. Xiao, C. Tang, J. Li, C. He, and J. Zhong, Potential thermoelectric material open framework Si₂₄ from a first-principles study, *J. Phys. D* **50**, 425501 (2017).
- [40] Y. Rao, C. Y. Zhao, and S. Ju, High thermoelectric performance in metastable phase of silicon: A first-principles study, *Appl. Phys. Lett.* **120**, 163901 (2022).
- [41] P.-H. Du and J. Zhou, Thermal property and lattice thermal conductivity of three-dimensional pentagonal silicon, *Phys. B: Condens. Matter* **618**, 413178 (2021).
- [42] H. Shao, D. Ding, L. Zhang, C.-K. Dong, and H. Zhang, Thermoelectric performance in a Si allotrope with ultralow thermal conductivity: a first-principles study combining phonon-limited electronic transport calculations, *Mater. Today Phys.* **27**, 100756 (2022).
- [43] H. Babaei, P. Keblinski, and J. M. Khodadadi, Thermal conductivity enhancement of paraffins by increasing the alignment of molecules through adding CNT/graphene, *Int. J. Heat Mass Transf.* **58**, 209 (2013).
- [44] J. Behler and M. Parrinello, Generalized Neural-Network Representation of High-Dimensional Potential-Energy Surfaces, *Phys. Rev. Lett.* **98**, 146401 (2007).
- [45] N. Fortier, J. Sheppard, and S. Strasser, Abductive inference in Bayesian networks using distributed overlapping swarm intelligence, *Soft Comput.* **19**, 981 (2015).

- [46] C. Peter and S. Matthew, Scalable variational inference for bayesian variable selection in regression, and its accuracy in genetic association studies, *Bayesian Anal.* **7**, 73 (2012).
- [47] T. M. Fragoso, W. Bertoli, and F. Louzada, Bayesian model averaging: A systematic review and conceptual classification, *Int. Stat. Rev.* **86**, 1 (2018).
- [48] See Supplemental Material at <http://link.aps.org/supplemental/10.1103/PhysRevMaterials.7.033803> for the lattice thermal conductivity of *d*-Si based on FMLP trained under MD simulations with different total steps, the per-atom energy, atomic force, and room temperature lattice thermal conductivity for Silicene and 2H-Si, which includes Refs. [70–73], the comparison of single point energy calculation time based on DFT and FMLP, the input parameters for searching for silicon allotropes using RG², which includes Refs. [49,74], the basic information (per-atom energy, space group, density, band gap type, lattice thermal conductivity in three directions) of *d*-Si, Si₂₄, and 102 novel metastable silicon crystal structures, the dependence of the lattice thermal conductivity and temperature in the three directions, the detailed atomic structure information, per-atom energy and atomic force, and detailed process of verifying the mechanical stability of *Cmcm*-Si₁₆, *P6/mmm*-Si₃₆₋₂, and *Pnma*-Si₃₂₋₂, which includes Ref. [75], the phonon mode information for *P6/mmm*-Si₃₆₋₂ and *Pnma*-Si₃₂₋₂.
- [49] X. Shi, C. He, C. J. Pickard, C. Tang, and J. Zhong, Stochastic generation of complex crystal structures combining group and graph theory with application to carbon, *Phys. Rev. B* **97**, 014104 (2018).
- [50] P. E. Blöchl, Projector augmented-wave method, *Phys. Rev. B* **50**, 17953 (1994).
- [51] A. V. Krugau, O. A. Vydrov, A. F. Izmaylov, and G. E. Scuseria, Influence of the exchange screening parameter on the performance of screened hybrid functionals, *J. Chem. Phys.* **125**, 224106 (2006).
- [52] J. P. Perdew, K. Burke, and M. Ernzerhof, Generalized Gradient Approximation Made Simple, *Phys. Rev. Lett.* **77**, 3865 (1996).
- [53] D. J. Chadi, Special points for Brillouin-zone integrations, *Phys. Rev. B* **16**, 1746 (1977).
- [54] V. Wang, N. Xu, J.-C. Liu, G. Tang, and W.-T. Geng, VASPKIT: A user-friendly interface facilitating high-throughput computing and analysis using VASP code, *Comput. Phys. Commun.* **267**, 108033 (2021).
- [55] D. Y. Kim, S. Stefanoski, O. O. Kurakevych, and T. A. Strobel, Synthesis of an open-framework allotrope of silicon, *Nat. Mater.* **14**, 169 (2015).
- [56] A. Togo and I. Tanaka, First principles phonon calculations in materials science, *Scr. Mater.* **108**, 1 (2015).
- [57] W. Li, L. Lindsay, D. A. Broido, D. A. Stewart, and N. Mingo, Thermal conductivity of bulk and nanowire Mg₂Si_xSn_{1-x} alloys from first principles, *Phys. Rev. B* **86**, 174307 (2012).
- [58] J. Tersoff, Modeling solid-state chemistry: Interatomic potentials for multicomponent systems, *Phys. Rev. B* **39**, 5566 (1989).
- [59] L. Weber and E. Gmelin, Transport properties of silicon, *Appl. Phys. A* **53**, 136 (1991).
- [60] Z. Han, X. Yang, W. Li, T. Feng, and X. Ruan, Four-Phonon: An extension module to ShengBTE for computing four-phonon scattering rates and thermal conductivity, *Comput. Phys. Commun.* **270**, 108179 (2022).
- [61] A. Jain, S. Ong, G. Hautier, W. Chen, W. Richards, S. Dacek, S. Cholia, D. Gunter, D. Skinner, G. Ceder, and K. Persson, Commentary: The materials project: A materials genome approach to accelerating materials innovation, *APL Mater.* **1**, 011002 (2013).
- [62] C. Liu, Z. Chen, C. Wu, J. Qi, M. Hao, P. Lu, and Y. Chen, Large thermal conductivity switching in ferroelectrics by electric field-triggered crystal symmetry engineering, *ACS Appl. Mater. Interfaces* **14**, 46716 (2022).
- [63] K. D. Parrish, A. Jain, J. M. Larkin, W. A. Saidi, and A. J. H. McGaughey, Origins of thermal conductivity changes in strained crystals, *Phys. Rev. B* **90**, 235201 (2014).
- [64] Z. Qin, G. Qin, X. Zuo, Z. Xiong, and M. Hu, Orbitally driven low thermal conductivity of monolayer gallium nitride (GaN) with planar honeycomb structure: A comparative study, *Nanoscale* **9**, 4295 (2017).
- [65] W. Humphrey, A. Dalke, and K. Schulten, VMD: Visual molecular dynamics, *J. Mol. Graphics* **14**, 33 (1996).
- [66] S. Maintz, V. L. Deringer, A. L. Tchougréeff, and R. Dronskowski, Analytic projection from plane-wave and PAW wavefunctions and application to chemical-bonding analysis in solids, *J. Comput. Chem.* **34**, 2557 (2013).
- [67] R. Nelson, C. Ertural, J. George, V. L. Deringer, G. Hautier, and R. Dronskowski, LOBSTER: Local orbital projections, atomic charges, and chemical-bonding analysis from projector-augmented-wave-based density-functional theory, *J. Comput. Chem.* **41**, 1931 (2020).
- [68] S. Y. Zhang, Y. L. Huang, C. Y. Wu, J. C. Han, L. Sun, and H. R. Gong, Effects of bond strength on the electronic structure and thermoelectric properties of β -VA monolayers (Sb, As, and P), *ChemNanoMat* **8**, e202100512 (2022).
- [69] N. Jia, J. Cao, X. Y. Tan, J. Dong, H. Liu, C. K. I. Tan, J. Xu, Q. Yan, X. J. Loh, and A. Suardi, Thermoelectric materials and transport physics, *Mater. Today Phys.* **21**, 100519 (2021).
- [70] Z. Liu, X. Wu, and T. Luo, The impact of hydrogenation on the thermal transport of silicene, *2D Mater.* **4**, 025002 (2017).
- [71] X. Gu and R. Yang, First-principles prediction of phononic thermal conductivity of silicene: A comparison with graphene, *J. Appl. Phys.* **117**, 025102 (2015).
- [72] B. Peng, H. Zhang, H. Shao, Y. Xu, G. Ni, R. Zhang, and H. Zhu, Phonon transport properties of two-dimensional group-IV materials from *ab initio* calculations, *Phys. Rev. B* **94**, 245420 (2016).
- [73] X. Gu and C. Y. Zhao, Thermal conductivity of hexagonal Si, Ge, and Si_{1-x}Ge_x alloys from first-principles, *J. Appl. Phys.* **123**, 185104 (2018).
- [74] C. He, X. Shi, S. J. Clark, J. Li, C. J. Pickard, T. Ouyang, C. Zhang, C. Tang, and J. Zhong, Complex Low Energy Tetrahedral Polymorphs of Group IV Elements from First Principles, *Phys. Rev. Lett.* **121**, 175701 (2018).
- [75] Z.-J. Wu, E.-J. Zhao, H.-P. Xiang, X.-F. Hao, X.-J. Liu, and J. Meng, Crystal structures and elastic properties of superhard IrN₂ and IrN₃ from first principles, *Phys. Rev. B* **76**, 054115 (2007).